Delft University of Technology

Using a flamelet generated manifold method in transported probability density function modeling of soot formation and thermal radiation

Stoellinger, Michael; Roekaerts, Dirk

DOI
10.1016/j.compfluid.2022.105567

Publication date
2022

Document Version
Final published version

Published in
Computers and Fluids

Citation (APA)
Stoellinger, M., & Roekaerts, D. (2022). Using a flamelet generated manifold method in transported probability density function modeling of soot formation and thermal radiation. *Computers and Fluids*, *245*, Article 105567. https://doi.org/10.1016/j.compfluid.2022.105567

Important note
To cite this publication, please use the final published version (if applicable).
Please check the document version above.

Copyright
Other than for strictly personal use, it is not permitted to download, forward or distribute the text or part of it, without the consent of the author(s) and/or copyright holder(s), unless the work is under an open content license such as Creative Commons.

Takedown policy
Please contact us and provide details if you believe this document breaches copyrights.
We will remove access to the work immediately and investigate your claim.

This work is downloaded from Delft University of Technology.
For technical reasons the number of authors shown on this cover page is limited to a maximum of 10.

Green Open Access added to TU Delft Institutional Repository

'You share, we take care!' - Taverne project

https://www.openaccess.nl/en/you-share-we-take-care

Otherwise as indicated in the copyright section: the publisher
is the copyright holder of this work and the author uses the
Dutch legislation to make this work public.

Computers and Fluids 245 (2022) 105567

Contents lists available at ScienceDirect

Computers and Fluids

journal homepage: www.elsevier.com/locate/compfluid

Using a flamelet generated manifold method in transported probability density function modeling of soot formation and thermal radiation

Michael Stoellinger [a,*], Dirk Roekaerts [b]

[a] *Department of Mechanical Engineering, University of Wyoming, 1000 East University Avenue, Laramie, WY 82071, USA*
[b] *Department of Process and Energy, Delft University of Technology, The Netherlands*

ARTICLE INFO

Keywords:
Chemistry Reduction
PDF modeling
Soot formation
Turbulence–Radiation-Interaction
Flamelet Generated Manifold

ABSTRACT

The simple semi-empirical precursor soot model of Brookes and Moss based on the soot number density and soot mass concentration is adopted in a transported probability density function (PDF) method for turbulent diffusion flames. The gas phase chemistry is described by a flamelet generated manifold (FGM) based on the mixture fraction, progress variable and enthalpy loss. The accuracy of the FGM method is validated by using flamelet solutions that are not included in the generating set of the FGM. To account for the radiative heat transfer in the flames, we use a non-gray weighted sum of gray gases model for the gas radiation and a gray soot radiation model. Turbulence–radiation interaction is closed at the level of the optically thin fluctuation approximation and the Reynolds averaged radiative transfer equation is solved by means of a discrete transfer method. The proposed modeling approach is applied in simulations of two turbulent non-premixed methane–air flames at one bar and three bar pressure, respectively. Predictions of the mean temperature and mean soot volume fraction are in good agreement with the measurements in the one bar flame. In the higher pressure flame the mean soot volume fraction is over predicted. For this flame, simulation results using the semi-empirical model of Lindstedt provided better agreement with the measurements. The main difference between the Brookes and Moss model and the Lindstedt model is the nine-times increased soot particle agglomeration rate of the latter. When using the same increased agglomeration rate parameter in the Brookes and Moss model the results become virtually identical. The negligible molecular diffusion of the soot was accounted for by neglecting mean molecular diffusion of the soot variables and by greatly reducing their micro-mixing. The effect of this differential soot diffusion on the mean soot volume fraction is found to be small, but it is significant for the variance of the soot volume fraction.

1. Introduction

Soot formation is a complex multi-scale process that involves both homogeneous and heterogeneous reactions as well as physical processes such as coagulation and agglomeration. The linking between the gas phase kinetics and soot kinetics is of great importance [1] and is commonly done through PAH species that form the soot precursors. The use of detailed soot models requires therefore sufficiently complex chemical mechanism that include PAH species. Detailed models for soot formation and oxidation have been developed and successfully applied in laminar flames [2–4].

The general applicability of detailed soot models in studies of turbulent flames using the transported probability density function (TPDF) method has first been demonstrated by Lindstedt and Louloudi [5]. More recently, Mehta et al. [6] used the TPDF method together with a Photon/Monte Carlo radiation model to predict soot formation in moderately sooting flames. The presence of soot greatly increases the emission and absorption of thermal radiation. Sufficiently complex radiation models are therefore required to predicted moderately and strongly sooting flames. The success of TPDF methods in predicting soot formation in turbulent flames is based on the closed treatment of the chemical source terms of the gas phase species and soot variables. However, the closed treatment of turbulence–chemistry interaction comes at a high computational cost in particular for detailed soot models that require large chemical mechanisms.

To reduce the computational cost, simpler semi-empirical precursor [7] soot models have been developed [8]. Such models are usually based on transport equations for the first two moments of the soot particle size distribution: the soot particle number density and the soot mass concentration. The gas phase soot precursor is acetylene C_2H_2 and the main oxidizing species is OH. To use the semi-empirical

---

* Corresponding author.
E-mail addresses: mstoell@uwyo.edu (M. Stoellinger), d.j.e.m.roekaerts@tudelft.nl (D. Roekaerts).

https://doi.org/10.1016/j.compfluid.2022.105567
Received 19 November 2021; Received in revised form 6 May 2022; Accepted 20 June 2022
Available online 23 June 2022
0045-7930/© 2022 Elsevier Ltd. All rights reserved.

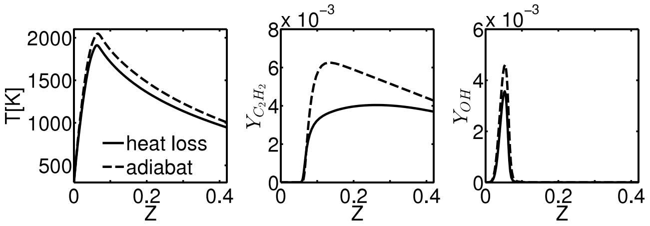

Fig. 1. Temperature (left), mass fraction of C_2H_2 (middle) and mass fraction of OH for a methane–air diffusion flamelet $a = 50\,\mathrm{s}^{-1}$ at $p = 1$ bar with heat loss (solid line) and adiabatic (dashed line).

soot model, one needs a chemical mechanism that includes C_2H_2 and OH as compared to the much larger PAH molecules. Hence much smaller chemical mechanisms can used. Moss et al. [8] used their semi-empirical soot model successfully with a simple flamelet model for the gas phase chemistry to predict soot formation in a two-dimensional laminar diffusion flame. The flamelet-soot model was later used to predict soot formation in turbulent methane–air diffusion flames at one bar and three bar pressure [9] using a presumed PDF method and with a TPDF model [10]. In the latter work, the joint PDF of mixture fraction, enthalpy loss, and soot variables (number density and mass concentration) was considered. Solving for the joint PDF significantly improved the results as compared to the presumed PDF results [9] since no modeling of the unknown correlations between soot variables and mixture fraction is required. Although the TPDF approach [10] provided improved results, there was still a significant deviation from the experimental results obtained by Brookes and Moss [11].

In the flamelet-soot model used by Aksit and Moss [10] in TPDF simulations, the heat loss due to thermal radiation does not change the chemical composition. The gas composition was “frozen” and only the temperature and density changed due to heat loss. This frozen chemistry approach for the heat loss in the chemistry model [10] is undesirable as it might introduce significant errors. Evidence for the inadequacy of the frozen chemistry approach for heat loss is provided in Fig. 1 where results for a laminar methane–air counter-flow diffusion flame (a flamelet) with a strain rate of $a = 50\,\mathrm{s}^{-1}$ at $p = 1$ bar under adiabatic conditions (dashed lines) and with heat loss (solid lines) are shown. Even for a moderate amount of heat loss of $\Delta T \approx 150$ K, that can easily occur through thermal radiation, the C_2H_2 mass fraction (responsible for soot nucleation and surface growth) is reduced by 40% and the OH mass fraction (main soot oxidation species) is reduce by 25%. Therefore, a better flamelet chemistry model that accounts for changes in composition due to heat loss should be used to predict soot formation.

In this work, we will adopt a tabulated chemistry approach based on the Flamelet Generated Manifold (FGM) method [12] that accounts for changes in chemical composition due to heat loss or gain. The accuracy of the FGM table is demonstrated by an “a priori” analysis. A similar tabulated chemistry model is adopted by Donde et al. [13] in the context of a Large Eddy Simulation/PDF method applied to predict soot formation in a weakly sooting non-premixed natural gas–air flame. In their work [13], they used a more complicated soot model based on PAH as the precursor and due to the small amount of soot only the emission of thermal radiation was accounted for. Here, the FGM method is used with the semi-empirical soot model [10] to predict soot formation in two laboratory scale non-premixed methane–air flames at atmospheric conditions and at elevated pressure [11]. The TPDF method is used to account for the effects of turbulence on the gas phase composition and soot kinetics. Radiative heat transfer is modeled with a Discrete Transfer Method (DTM) [14] and hence emission as well as re-absorption of thermal radiation are counted for. Most previous numerical studies of the Brookes and Moss flames [9,10,15] only accounted for radiative heat loss through emission. Consalvi et al. [16] accounted for self-absorption by solving the radiative transfer equation with a finite volume method using a wide-band correlated-k spectral model for gas and soot radiation. The chemistry was modeled with a simpler steady flamelet model with enthalpy defect [16,17].

The paper is organized as follows. A brief summary of the laboratory flames is given in Section 2 and the FGM model for these flame is presented in Section 3. The TPDF modeling approach is presented in Section 4 and some simulation details are provided in Section 5. The simulation results are presented in Section 6.

2. Brookes and Moss methane–air flames

Brookes and Moss [11] performed measurements of the mean temperature, mean mixture fraction and mean soot volume fraction in two turbulent methane–air diffusion flames at $p = 1$ bar and $p = 3$ bar. The burner consists of a central fuel jet with nozzle diameter $D = 4.07$ mm, surrounded by a concentric co-flow of air. Premixed methane–air pilot flames, which are necessary to stabilize the flame on the burner, are issued from holes located on a rim separating the air flow from the fuel flow. The air annulus consists of a Pyrex tube with outer diameter of 155 mm. The methane is issued from the fuel jet nozzle at a flow rate of $\dot{m}_{\mathrm{CH}_4} = 1.72 \cdot 10^{-4}$ kg/s which implies an exit velocity of $U_f = 20.3$ m/s for the one bar flame and $U_f = 6.8$ m/s for the three bar flame. The co-flow air velocities are given by $U_a = 0.61$ m/s and $U_a = 0.186$ m/s for the one and three bar flames, respectively, resulting in a global equivalence ratio of 0.25 in both flames and a Reynolds number based on the fuel nozzle diameter of Re = 5000. Both streams are kept at approximately $T = 295$ K. In the following, the one bar flame will be referred to as P1 and the three bar flame as P3.

Given the fairly small Reynolds number and the small exit velocity in particular in the flame P3 it is instructive to estimate the relevance of buoyancy effects. The densimetric Froude number provides a good measure of the relevance of buoyancy [18] and is defined by

$$Fr = \frac{\rho_j U_j^2}{g D_j |\rho_a - \rho_j|}, \tag{1}$$

where ρ_j, U_j, D_j are the density, the bulk velocity and the diameter of the jet, ρ_a is the density of the ambient fluid and $g = 9.81$ m/s^2 is the gravitational acceleration. Assuming the density of the ambient combustion products to be $\rho_a = 0.3$ kg/m^3 for flame P1 and $\rho_a = 1$ kg/m^3 for flame P3 gives $Fr_{P1} = 18{,}400$ and $Fr_{P3} = 1180$ for the flame P1 and P3, respectively. The axial distance where buoyancy becomes relevant can be estimated to be $x_b = Fr^{1/2} \left(\rho_j/\rho_a\right)^{0.25} D/2$ [18] which leads to $x_{b1} = 335$ mm and $x_{b3} = 82$ mm. Therefore, buoyancy effects are expected to be relevant in particular for the flame P3. Details on the modeling of buoyancy effects is discussed in Section 4.

3. Tabulated chemistry model: Flamelet Generated Manifold (FGM) with heat loss/gain

The FGM is a low dimensional approximation of the high dimensional solution of non-premixed laminar flamelets in composition space. Using this approximation, the composition evolution is described by only a few variables for which the chemical source terms are tabulated leading to a significant reduction of the computational effort [12,19–21]. The FGM method has been extended to non-adiabatic conditions mostly to account for heat loss to walls [20,21]. However, these previous approaches are based on constant enthalpy flamelets and might thus not be valid when the cooling takes place in the active flame region [21] as is the case in sooting flames. A novel approach to account for radiative heat loss/gain using non-constant enthalpy flamelets is presented in the following. A strategy for the efficient storage of the resulting FGM in a three-dimensional table is also presented along with an assessment of the accuracy of the FGM table representation.

3.1. Generation of the FGM

For simple non-premixed adiabatic flames the first step in the creation of an FGM is to solve the steady state non-premixed laminar flamelet equations using a detailed chemical mechanism (for the methane–air combustion we use GRI 3.0 [22] including $N_s = 53$ species) for a range of different strain rates. A reaction progress variable Y is defined based on a linear combination of the mass fraction of the main combustion products:

$$Y = \frac{Y_{H_2}}{M_{H_2}} + \frac{Y_{H_2O}}{M_{H_2O}} + \frac{Y_{CO_2}}{M_{CO_2}}, \; S_Y = \frac{S_{Y_{H_2}}}{M_{H_2}} + \frac{S_{Y_{H_2O}}}{M_{H_2O}} + \frac{S_{Y_{CO_2}}}{M_{CO_2}}, \tag{2}$$

where Y_α denotes the mass fraction of species α, M_α denotes the molecular weight, S_α denotes the chemical source term (mass fraction based) and S_Y is the chemical source term of the progress variable. Based on the above definition, the units of the progress variable Y and its source term S_Y are [mol/kg] and [mol/(kg s)], respectively. If the laminar flamelet equations are solved in physical space x for different strain rates a the result for any thermo-chemical variable θ can be written as $\theta = \mathcal{G}_{flt}(x;a)$ where a is from the strain rate range. In the following we will consider the Bilger mixture fraction Z [23] such that $Z = 1$ in the pure fuel stream and $Z = 0$ in the air stream. Since $Z(x)$ is a monotonic function (assuming unity Lewis numbers) the results from physical space can be transformed into mixture fraction space. For a given mixture fraction value, the progress variable is a monotonic function of the strain rate (Y is increasing for decreasing strain rate values). Therefore, the strain rate parameter can be transformed into the progress variable and all the thermo-chemical data from the flamelet solutions (along with the S_Y) is stored in a two-dimensional table $\theta = \mathcal{G}_{FGM}(Z, Y)$. Using this table, the original problem of solving $N_s + 1 = 54$ partial differential equations could be reduced to solving only two equations: one for the conserved scalar Z and one for the reaction progress variable Y.

An extension of the flamelet strategy to account for emission-only radiative heat losses has been presented in [24] in the context of a flamelet/progress variable model. Here, we extend this approach to the FGM method and also account for enthalpy gain due to radiation which can occur locally if the radiation model accounts for emission and absorption (see Section 4). The starting point is a set of steady adiabatic counter-flow diffusion flamelet solutions for different strain rates: 12 values for the one bar flame a = [0.1, 1, 2, 5, 10, 20, 50, 70, 100, 200, 300, 400] s^{-1} and 14 values for the three bar flame a = [0.1, 1, 2, 5, 10, 20, 50, 70, 100, 200, 300, 400, 600, 900] s^{-1}. The maximum strain rate values are close to the extinction strain rates. Since both Brookes and Moss flames have a low Reynolds number, local extinction is not important and therefore only burning flamelets are considered.

The adiabatic steady flamelet solutions are used as initial conditions to obtain unsteady flamelet solutions with a sink term $\dot{q}_{rad,L}$ in the enthalpy equation that resembles radiative heat loss due to emission

$$\dot{q}_{rad,L} = -4\sigma\kappa c_R \left(T^4 - T_R^4\right), \tag{3}$$

where T is the temperature, $T_R = 295$ K the temperature of the environment, κ is the Planck mean absorption coefficient (based on CO_2, H_2O and CH_4 [25]), $\sigma = 5.67 \cdot 10^{-8}$ W/m^2 K^4 is the Stefan Boltzmann constant. A total of eight unsteady "cooling" solutions are stored until a steady state with heat loss is reached. The presence of soot strongly increases the absorption coefficient κ. Since the flamelet solutions do not include soot formation, the thin flamelets would only loose a small amount of heat. We artificially increase the absorption coefficient with the factor $c_R = 10$, thus creating flamelets with significant radiative heat loss. The value of this factor is somewhat arbitrary and it has to be adjusted for the turbulent flames of interest. As a guideline, it should be set large enough such that the maximum heat loss in the flamelet (i.e. the steady solution with heat loss) is larger than what is expected to occur in the target turbulent flame with the inclusion of radiation from the soot. The upper limit for the c_R factor is given by the condition that only "burning" flamelet solutions are considered for the FGM (i.e. flame extinction due to radiative heat loss is not considered). The unsteady cooling solutions at increasing times correspond to increasing levels of enthalpy loss. To be able to transform "increasing time" in the flamelet solutions into increasing enthalpy loss, an enthalpy deficit variable is introduced:

$$\Delta h(Z, t; a) = h(Z, t; a) - h_{ad}(Z), \quad h_{ad} = Z h_f + (1 - Z) h_a, \tag{4}$$

where h_f is the enthalpy of the methane fuel stream ($T_f = 295$ K) and h_a is the enthalpy of the air stream ($T_a = 295$ K).

To include the enthalpy gain due to absorption of thermal radiation, a constant heat source $\dot{q}_{rad,G} = 7 \cdot 10^4$ J/kg/m^3 is included in the enthalpy equation. Starting from the steady adiabatic initial conditions, unsteady solutions are stored until the temperature at the stoichiometric mixture fraction ($Z_{st} = 0.055$) has increased by 200 K. A total of three unsteady "heating" solutions are stored and used in the FGM. The exact value of $\dot{q}_{rad,G}$ is not very important as long as the desired amount of enthalpy gain is reached. All the laminar flamelet calculations have been performed in physical space using the 1D flame code CHEM1D [26] developed at the Eindhoven University of Technology using the GRI 3.0 chemical mechanism. The Lewis numbers of all species are set to unity and adaptive mesh refinement (150 grid points total) is used to resolve the strong gradients of species in physical space.

The steady adiabatic, the unsteady cooling, and the unsteady heating solutions at the different strain rates form the basis for the construction of the FGM. Using the mixture fraction Z, the reaction progress variable Y and the enthalpy deficit Δh the flamelet solutions are used to construct a three-dimensional FGM and the mapping $\theta = \mathcal{G}_{FGM}(Z, Y, \Delta h)$ is stored in a table for all thermochemical variables $\theta \in (T, \rho, \mu, S_Y, Y_\alpha)$. A piece wise uniform grid is chosen to discretize the mixture fraction space: 101 points are used in the range $Z = [0, Z_R = 0.1]$ and 21 points are used in $Z = (Z_R, 1]$. The flamelet solutions given in physical space are then transformed into mixture fraction space and mapped on the mixture fraction grid (using linear interpolation). Choosing Z_R about twice as large as the stoichiometric mixture fraction value $Z_{st} = 0.055$ allows to represent the flames up to the rich region (where most of the soot formation occurs) more accurately. For $Z > Z_R$ the thermochemical variables change very smoothly and hence the coarser grid is sufficient. The range of progress variable values $[Y_{min}(Z), Y_{max}(Z)]$ is discretized by $N_Y = 40$ equidistant points and the range of enthalpy deficit values $[\Delta h_{min}(Z), \Delta h_{max}(Z)]$ is discretized by $N_{\Delta h} = 200$ equidistant points. For all $(Z, Y, \Delta h)$ grid values that are not contained in the flamelet solutions linear interpolation is used.

The computer program FLAME [27] developed at the TU-Delft is used to perform the actual tabulation of the 3D-FGM. The FLAME tabulation code is used because it has adaptive grid refinement capability. Only the values of the thermo-chemical variables required in the actual CFD simulation (S_Y, ρ, μ, T, $X_{C_2H_2}$, X_{OH} and X_{O_2}) are stored in this table (X denotes molar fractions). The adaptive grid refinement is based on gradient and curvature criteria and allows to further "compress" the FGM data. In the FLAME code, the physical range of the three independent variables $(Z, Y, \Delta h)$ is mapped onto a cube $[0, 1]^3$ to facilitate the adaptive grid refinement. The reaction progress variable and the enthalpy deficit are normalized using

$$c = \frac{Y - Y_{min}(Z)}{Y_{max}(Z) - Y_{min}(Z)}, \; h_{sc} = \frac{\Delta h - \Delta h_{min}(Z)}{\Delta h_{max}(Z) - \Delta h_{min}(Z)} \tag{5}$$
$$c, h_{sc} \in [0, 1],$$

and $Y_{min}(Z)$, $Y_{max}(Z)$, $\Delta h_{min}(Z)$, and $\Delta h_{max}(Z)$ are also stored in the table. The look-up tables generated by FLAME have a size of 62Mb for the P1 case and 76Mb for the P3 case, respectively.

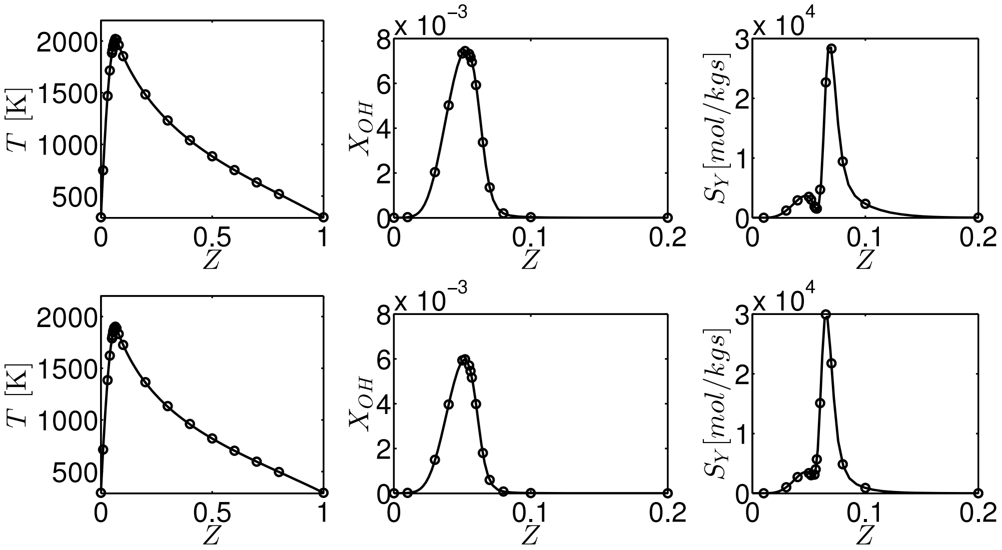

Fig. 2. Comparison between the original flamelet results (solid line) and the corresponding values retrieved from the FGM table (circles) for the one bar pressure case at adiabatic conditions (top row) and with heat loss (bottom row). The left plots shows the temperature, the center plots the OH mole fraction and the right plots show the source term of the progress variable.

3.2. Accuracy of the FGM tabulated chemistry

Several approximations are used in the generation of the FGM lookup table. The steady flamelet assumption, the limited number of flamelet solutions (strain rates and heat loss/gain) that form the basis of the FGM, the discretization of the $(Z, Y, \Delta h)$ space, and the linear interpolation operations are all contributing to an error in the representation of the chemistry. The quality of steady flamelet assumption has been validated by several researchers [24,28] and is not evaluated here. It should be noted that neither the P1 flame nor the P3 flame experience local extinction and hence the steady flamelet assumption is very reasonable. The accuracy of the FGM look-up tables is evaluated by retrieving data for a flamelet that is part of the set of flamelets that generates the FGM first. This evaluation reveals the errors due to the $(Z, Y, \Delta h)$ space discretization and the linear interpolation. The comparison is made for a strain rate of $a = 100$ s^{-1} for the one bar flame P1 and a strain rate of $a = 50$ s^{-1} for the three bar flame P3. These strain rate values are representative of the benign strain rates experienced in the turbulent flames.

Fig. 2 shows a comparison between the original flamelet results (solid line) and the corresponding values retrieved from the FGM table (circles) for the one bar pressure case at adiabatic conditions (top) and with heat loss (bottom). The maximum heat loss of this flamelet solution is $\Delta h_{max} = -287$ kJ/kg and occurs at a mixture fraction $Z = 0.197$. The comparison is shown for the temperature (left), the OH mole fraction (center) and the source term of the progress variable (right) evaluated at twenty mixture fraction values from the FGM table. The three variables are chosen because of their relevance for the soot predictions in the turbulent flame calculations and because they display quite different variations through the flame. The figure shows that the values retrieved from the FGM table match the original results very closely. To quantify the error between the original flamelet solution and the corresponding values retrieved from the FGM table we use the L^2-norm to define a relative error

$$\epsilon_x = \frac{\|\hat{x} - x\|_2}{\|\hat{x}\|_2}, \tag{6}$$

were x is the exact flamelet solution value (for T, X_{OH} or S_Y) and $\hat{x}$ denotes a value retrieved from the FGM table. The relative errors based on the twenty mixture fraction points are summarized in Table 1. For the one bar case the relative errors are below 2% and for the three bar case they are below 6%. The slightly larger relative errors in the three bar case most likely reflects the increased reactivity as compared to the one bar case. In both cases the errors are sufficiently small, thus it can be concluded that the FGM table represents the original flamelet data with sufficient accuracy.

Table 1
Relative errors between the flamelet solution and the FGM table representation as defined by Eq. (6) for a flamelet that is included in the generating set of the FGM table.

Flamelet case	ϵ_T	$\epsilon_{X_{OH}}$	ϵ_{S_Y}
One bar pressure			
$a = 100$ s^{-1} adiabat	0.04%	0.2%	1.9%
$a = 100$ s^{-1} with heat loss	0.1%	0.7%	1.8%
Three bar pressure			
$a = 50$ s^{-1} adiabat	0.06%	1.1%	5.9%
$a = 50$ s^{-1} with heat loss	0.6%	1.8%	4.4%

Table 2
Relative errors between the flamelet solution and the FGM table representation as defined by Eq. (6) for a flamelet that is not included in the generating set of the FGM table.

Flamelet case	ϵ_T	$\epsilon_{X_{OH}}$	ϵ_{S_Y}
One bar pressure			
$a = 85$ s^{-1} with heat loss	0.1%	0.3%	1.6%
Three bar pressure			
$a = 35$ s^{-1} with heat loss	0.29%	2.7%	4.9%

The ability of the FGM table to predict the composition and temperature of a flamelet solution that is not included in its "generating" set of flamelets is considered next. To this end, flamelets with significant heat loss are considered at strain rates of $a = 85$ s^{-1} and $a = 35$ s^{-1} for one and three bar pressure, respectively. Both strain rate values are half way between strain rate values that are included in the generating set. The results for the relative errors are summarized in Table 2. For both cases and for the three considered variables the relative error is below 5%. It is interesting to observe that the relative errors reported in Table 2 are overall slightly smaller than those in Table 1: this observation indicates that the error that is introduced by interpolating between two generating flamelets is smaller than the error that results from the discretization of the $(Z, Y, \Delta h)$ space. Hence, the discretization error is dominant and the accuracy of the FGM table could be improved by using a finer discretization. However, the relative errors for the adopted

FGM tables are sufficiently small and hence further refinement is not considered in this work.

4. Modeling strategy

4.1. Soot model

The semi empirical precursor model of Brookes and Moss [8,10] for soot formation based on the soot mass concentration $M = \rho Y_s$ and the normalized particle number density $N = n/N_A = \rho N_s$ (with N_A the Avogadro constant) is adopted in this work. This two-equation soot model is well established and it is also available in commercial CFD codes such as ANSYS FLUENT [29]. Note that the actually transported soot scalars are the soot mass fraction $Y_s = M/\rho$ and the specific soot particle number $N_s = N/\rho$.

The soot particles are assumed to be spherical and have a size distribution that can be satisfactorily represented by the average diameter:

$$D = \left(\frac{6M}{\pi \rho_{soot} n} \right)^{1/3} \tag{7}$$

Soot nucleation and surface growth are governed by the acetylene mole fraction $X_{C_2H_2}$. Following the suggestion of [10,15], oxidation due to O_2 and OH is accounted for. It should be noted here that the adopted soot model corresponds to the soot model developed by Moss et al. [8] for laminar flames. No additional scaling parameters are introduced and the same soot model is used in the flames P1 and P3. The resulting source term for the normalized soot number density N is repeated here for completeness

$$\begin{aligned} \dot{N} = {} & C_\alpha \frac{X_{C_2H_2} p}{RT} \exp\left(\frac{-T_{An}}{T} \right) \\ & - \left[C_a \left(\frac{24RT}{\rho_{soot} N_A} \right)^{1/2} \left(\frac{6}{\rho_{soot} \pi} \right)^{1/6} N_A^{5/6} \right] \cdot M^{1/6} \cdot N^{11/6}, \end{aligned} \tag{8}$$

and the source term for the soot mass concentration is

$$\begin{aligned} \dot{M} = {} & M_P C_\alpha \frac{X_{C_2H_2} p}{RT} \exp\left(\frac{-T_{An}}{T} \right) \\ & + \left[C_\gamma \frac{X_{C_2H_2} p}{RT} \exp\left(\frac{-T_{As}}{T} \right) (\pi N_A)^{1/3} \left(\frac{6}{\rho_{soot}} \right)^{2/3} \right] \cdot M^{2/3} \cdot N^{1/3} \\ & - C_{\omega 1} \frac{X_{OH} p}{RT} \sqrt{T} (\pi N_A)^{1/3} \left(\frac{6}{\rho_{soot}} \right)^{2/3} \cdot M^{2/3} N^{1/3} \\ & - C_{\omega 2} \frac{X_{O_2} p}{RT} \sqrt{T} \exp(-T_{Ao}/T) (\pi N_A)^{1/3} \left(\frac{6}{\rho_{soot}} \right)^{2/3} \cdot M^{2/3} N^{1/3}. \end{aligned} \tag{9}$$

The model constants according to [10] are given by: $M_P = 144$ kg/kmol, $T_{An} = 21,100$ K, $T_{As} = 12,100$ K, $T_{Ao} = 19,800$ K, $C_\alpha = 54$ s^{-1}, $C_a = 1$, $C_\gamma = 11.7 \cdot 10^3$ m^{-2} s^{-1}, $C_{\omega 1} = 4.2325$ and $C_{\omega 2} = 8903$. The soot solid density is $\rho_{soot} = 1800$ kg/m^3 [10] and the soot volume fraction f_v can thus be calculated as $f_v = M/\rho_{soot} = \rho Y_s/\rho_{soot}$. The pressure p is constant and is set to one bar for the flame P1 and to 3 bar for the flame P3.

4.2. Radiation model

In sooting flames, radiative heat transfer is often a main mechanism of heat transfer between the hot gas-soot mixture and the surrounding medium. The participating combustion product gases H_2O and CO_2 have a very complex dependence of the spectral absorption coefficient with the wavenumber [30,31]. The spectral absorption coefficient of soot has a simpler near-linear dependence on the wavenumber but it is still a non-gray participating specie [30,31]. Soot is formed on the rich side of the flame and the soot volume fraction varies significantly throughout a flame. For methane flames, the highest observed soot volume fraction values are typically between 0.1–10 ppm. For such modest soot loading, it has been shown that the radiative contribution of soot can be reasonably approximated with a gray model [32].

A large number of models for non-gray thermal radiation in combustion problems has been developed and an excellent review is provided in [30]. A computationally very efficient model for H_2O, CO_2 and soot mixtures is the weighted-sum-of-gray-gases (WSGG) model [31–35]. Here, we use the WSGG coefficients of Bordbar et al. [35] for H_2O-CO_2 mixtures with varying molar ratios. This model includes four gray gases ($N_g = 4$) and one clear gas. The ith gray gas absorption coefficients are given by (the clear gas has $\kappa_{g,0} = 0$)

$$\kappa_{g,i}(p_{atm}, X_{H_2O}, X_{CO_2}) = p_{atm} \cdot \left(X_{H_2O} + X_{CO_2} \right) \sum_{k=0}^{4} d_{i,k} M_r^k, \ \forall i = 1, \dots, N_g \tag{10}$$

where p_{atm} is the pressure in atmospheres, d_{ik} are model coefficients given in [35], and $M_r = \frac{X_{H_2O}}{X_{CO_2}}$ is the local molar ratio which is limited to the range $0.1 \le M_r \le 4$ [35]. Soot is modeled as gray specie with a Planck-mean absorption coefficient given by [32]

$$\begin{aligned} & \kappa_s(f_v, T) = f_v \left(a \cdot T^3 + b \cdot T^2 + c \cdot T + d \right) \\ & \quad a = 2.156 \cdot 10^{-5} \ \mathrm{K^{-3} m^{-1}}, b = -0.2889 \ \mathrm{K^{-2} m^{-1}}, \\ & \quad c = 1804 \ \mathrm{K^{-1} m^{-1}}, d = 2.012 \cdot 10^5 \mathrm{m^{-1}}, \end{aligned} \tag{11}$$

where f_v is the local soot volume fraction given by M/ρ_{soot} and T is the temperature, respectively.

For the considered non-gray gas WSGG model with a gray soot model, the following radiative heat transfer equations (RTE) for each of the gray gas intensities I_i are solved [31,32,34]

$$\frac{dI_i}{ds} = -\left(\kappa_{g,i} + \kappa_s \right) I_i + a_i \left(\kappa_{g,i} + \kappa_s \right) \frac{\sigma T^4}{\pi}, \ \forall i = 0, \dots, N_g, \tag{12}$$

where a_i are weight factors for the emission of each gray gas which are given by

$$a_i(T, X_{H_2O}, X_{CO_2}) = \sum_{j=0}^{4} b_{i,j} T_r^j \, , b_{i,j} = \sum_{k=0}^{4} C_{i,j,k} M_r^k, \forall i = 1, \dots, N_g. \tag{13}$$

Here, a reduced temperature $T_r = T/1200$ K is used and the coefficients $C_{i,j,k}$ can be found in [35]. The weight for the clear gas is found from $a_0 = 1 - \sum_{i=1}^{N_g} a_i$. The total incident radiation is then obtained from the gas intensities by

$$G = \sum_{i=0}^{N_g} \int I_i d\Omega, \tag{14}$$

where the integration is over all solid angles.

In RANS modeling of turbulent combustion, the instantaneous RTE needs to be Reynolds averaged to account for turbulence–radiation interaction (TRI) [30,36]. The absorption term is then given by $\langle \left(\kappa_{g,i} + \kappa_s \right) I_i \rangle = \langle \kappa_{g,i} + \kappa_s \rangle \langle I_i \rangle + + \langle \left(\kappa'_{g,i} + \kappa'_s \right) I'_i \rangle$. The correlation between the absorption coefficient and radiative intensity fluctuations has been shown to be small [6,36] for the moderately sooting laboratory flames studied here. This assumption is commonly referred to as the optically thin fluctuation approximation (OTFA) [30,36,37] and the averaged RTE's to be solved are

$$\frac{d\langle I_i \rangle}{ds} = -\langle \kappa_{g,i} + \kappa_s \rangle \langle I_i \rangle + \left\langle a_i \left(\kappa_{g,i} + \kappa_s \right) \frac{\sigma T^4}{\pi} \right\rangle, \ \forall i = 0, \dots, N_g. \tag{15}$$

The correlations in the emission term are all one-point statistics and can easily be calculated in the adopted composition PDF-RANS method. However, storage requirements are increased as averages for a total of ten additional fields need to be stored.

A computationally economic method of solving the radiative heat transfer equation (RTE) is the discrete transfer method (DTM) [14,38]. The DTM is based on the numerical solution of the RTE along specified directions. Here, we adopt the nearly-conservative formulation of Coelho and Carvalho [38]. We use the DTM since it is highly efficient when the beam paths are pre-calculated as is done in our implementation. The DTM is not strictly conservative but neither are finite volume Discrete Ordinate Methods that use upwind biased flux methods. Due to the high efficiency of the DTM, we are able to use a large number of rays (16,384 from each boundary face) which greatly reduces the ray-effect and we find a global conservation error of less than 0.1% (i.e. the difference between the surface integral of the boundary heat flux and the volume integral of the source term). More details about the solution strategy of the DTM can be found in [37].

4.3. Turbulence–chemistry interaction

The independent scalar variables considered are the mixture fraction Z, the progress variable Y, the total specific enthalpy h, the normalized specific soot number N_s and the soot mass fraction Y_s. The joint PDF of the scalar variables $\boldsymbol{\phi} = [Z, Y, h, N_s, Y_s]$ is obtained by a hybrid composition PDF-RANS method [39–41]. The PDF equation is solved by a Monte Carlo method for notional particles. The position of the stochastic particles evolves according to [40]

$$dx_i^* = \left(\left[\widetilde{u}_i\right]^* + \frac{1}{\left[\langle\rho\rangle\right]^* Sc_t} \left[\frac{\partial\langle\rho\rangle\, \nu_t}{\partial x_i}\right]^* \right) dt + \sqrt{\frac{2\nu_t}{Sc_t}} dW_i, \tag{16}$$

Here, $[]^*$ denotes that the variable is interpolated to the particles position and dW_i denotes the increment of the ith component of a vectorial Wiener process. The increments dW_i are Gaussian random variables which are determined by their first two moments,

$$\langle dW_i \rangle = 0, \ \left\langle dW_i dW_j \right\rangle = \delta_{ij} dt. \tag{17}$$

The Favre mean velocity $\widetilde{u}_i$ and the turbulent viscosity ν_t are obtained from the finite-volume RANS solver (see Section 4.4) and are then interpolated onto the particles position [37,41]. The turbulent Schmidt number is given by $Sc_t = 0.6$.

The micro-mixing of the scalars is modeled by the Interaction by Exchange with the Mean (IEM) mixing model. The evolution of the scalars ϕ_α is given by

$$d\phi_\alpha^* = \frac{\partial}{\partial x_k} \left(\frac{\langle \nu \rangle}{Sc_\alpha} \frac{\partial \tilde{\phi}_\alpha}{\partial x_k} \right) dt - \frac{\omega_\alpha}{2} \left(\phi_\alpha^* - \tilde{\phi}_\alpha \right) dt + S_\alpha \cdot dt, \tag{18}$$

where the first term accounts for the mean molecular diffusion. The laminar Schmidt numbers for the mixture fraction, progress variable and enthalpy are set to $Sc = 0.7$. Since the molecular diffusion of the soot is negligible, $Sc \to \infty$ is used for the soot variables N_s, Y_s. The scalar mixing frequency is given by $\omega_\alpha = C_\phi \frac{\varepsilon}{k}$ with $C_\phi = 2.0$ for the gaseous scalars Z, Y, h. To account for the negligible molecular mixing of the soot scalars, the scalar mixing frequency for the soot variables is reduced by a factor $C_{ms} = 100$ such that $\omega_s = \omega_\phi / C_{ms}$. A similar approach was adopted in [16] were mixing of the soot variables was also neglected. The influence of the chosen value for C_{ms} is investigated in Section 6.3.

The mixture fraction Z is treated as a conserved scalar and hence it has no source term. This implies that mass transfer from the gaseous to the solid "soot" state is neglected (no source term in the gas continuity equation). This is a reasonable assumption for the moderately sooting flames under consideration. The source term for the reaction progress variable S_Y is obtained from the look-up table. The numerical integration of the source term uses a third order Runge–Kutta method with an error control so that the time-step is reduced if required. Therefore, the source term has to be retrieved at least three times for each time step. The source term for the specific enthalpy is due to thermal radiation and is given by

$$S_h = \frac{1}{\rho^*} \left[\left(\kappa_{g,i}^* + \kappa_s^* \right) \left[\langle G \rangle\right]^* - 4\sigma \left(\kappa_{g,i}^* + \kappa_s^* \right) a_i^* T^{*4} \right], \tag{19}$$

where $\langle G \rangle$ is the average incident radiation which is obtained from the solution of the averaged radiative transfer equation. The enthalpy source term is integrated with an explicit Euler method for each particle. The source terms for the soot variables $S_{N_s} = \dot{N}/\rho^*$ and $Y_s = \dot{M}/\rho^*$ depend also on the gas phase scalars and they are integrated with an implicit Euler method.

To find the dependent thermo-chemical variables such as the ρ^*, T^*, $X^*_{C_2H_2}$, and X^*_{OH}, the lookup table is entered with (Z^*, Y^*, h^*) and the required variables are retrieved (see Section 3 for details).

4.4. RANS finite volume model

In the adopted hybrid composition PDF-RANS method the mean velocity field $\widetilde{u}_i$, the mean pressure $\langle p \rangle$, the Reynolds stress $\widetilde{u_i'' u_j''}$ and the mean dissipation rate ε are obtained by solving the corresponding modeled transport equations with a finite volume method. The Favre averaged Navier Stokes equations are given by

$$\frac{\partial \langle \rho \rangle}{\partial t} + \frac{\partial \langle \rho \rangle \widetilde{u}_i}{\partial x_i} = 0, \tag{20}$$

and

$$\begin{aligned} \frac{\partial \langle \rho \rangle \widetilde{u}_i}{\partial t} + \frac{\partial \langle \rho \rangle \widetilde{u}_j \widetilde{u}_i}{\partial x_j} = &- \frac{\partial \langle p \rangle}{\partial x_i} + \frac{\partial}{\partial x_j} \left[\langle \rho \rangle \widetilde{\nu} \left(\frac{\partial \widetilde{u}_i}{\partial x_j} \right) \right] \\ &- \frac{\partial \langle \rho \rangle \widetilde{u_i'' u_j''}}{\partial x_j} + \langle \rho \rangle g_i, \end{aligned} \tag{21}$$

where $\widetilde{\nu}$ denotes the Favre averaged kinematic viscosity and g_i is the gravitational acceleration. The mean density $\langle \rho \rangle$ is obtained from the Monte Carlo solver [39]. The Reynolds stress model is based on the isotropization of production model developed by Launder [42] and is given by

$$\begin{aligned} \frac{\partial \langle \rho \rangle \widetilde{u_i'' u_j''}}{\partial t} + \frac{\partial \langle \rho \rangle \widetilde{u}_k \widetilde{u_i'' u_j''}}{\partial x_k} = &\frac{\partial}{\partial x_k} \left[C_s \langle \rho \rangle \frac{k}{\varepsilon} \widetilde{u_k'' u_l''} \frac{\partial \widetilde{u_i'' u_j''}}{\partial x_l} \right] \\ &+ P_{ij} + P_{b,ij} + \boldsymbol{\Phi}_{ij} - \frac{2}{3} \langle \rho \rangle \varepsilon \delta_{ij}, \end{aligned} \tag{22}$$

where the production of stress due to mean velocity gradients is given by

$$P_{ij} = - \langle \rho \rangle \left(\widetilde{u_i'' u_k''} \frac{\partial \widetilde{u}_j}{\partial x_k} + \widetilde{u_j'' u_k''} \frac{\partial \widetilde{u}_i}{\partial x_k} \right), \tag{23}$$

and the production of stress due to Buoyancy is given by

$$P_{b,ij} = - \frac{\nu_t}{Sc_t} \left(g_i \frac{\partial \langle \rho \rangle}{\partial x_j} + g_j \frac{\partial \langle \rho \rangle}{\partial x_i} \right). \tag{24}$$

The pressure–strain correlation is modeled by

$$\begin{aligned} \boldsymbol{\Phi}_{ij} = &- \langle \rho \rangle C_1 \frac{\varepsilon}{k} \left(\widetilde{u_i'' u_j''} - \frac{2}{3} \delta_{ij} k \right) \\ &- C_2 \left(P_{ij} - \frac{1}{3} \delta_{ij} P_{kk} \right). \end{aligned} \tag{25}$$

The model coefficients are given by $C_s = 0.22$, $C_1 = 1.8$ and $C_2 = 0.6$. The dissipation rate of turbulent kinetic energy is provided according to the standard modeled transport equation with an additional round jet correction proposed by Pope [43]

$$\begin{aligned} \frac{\partial \langle \rho \rangle \varepsilon}{\partial t} + \frac{\partial \langle \rho \rangle \widetilde{u}_j \varepsilon}{\partial x_j} = &\frac{\partial}{\partial x_j} \left[C_{s\varepsilon} \langle \rho \rangle \frac{k}{\varepsilon} \widetilde{u_j'' u_k''} \frac{\partial \varepsilon}{\partial x_k} \right] + \frac{\varepsilon}{k} C_{\varepsilon 1} P_{kk} \\ &- \langle \rho \rangle \frac{\varepsilon^2}{k} \left(C_{\varepsilon 2} - S_\varepsilon \right). \end{aligned} \tag{26}$$

The round jet correction in the adopted cylindrical coordinate system is given by

$$S_\varepsilon = \frac{C_{\varepsilon 3}}{4} \left(\frac{k}{\varepsilon} \right)^3 \left(\frac{\partial \widetilde{u}_1}{\partial x_2} - \frac{\partial \widetilde{u}_2}{\partial x_1} \right)^2 \frac{\widetilde{u}_2}{r}. \tag{27}$$

The model coefficients are given by $C_{s\varepsilon} = 0.18$, $C_{\varepsilon 1} = 1.44$, $C_{\varepsilon 2} = 1.92$ and $C_{\varepsilon 3} = 0.79$. The turbulent viscosity that is required in the Monte-Carlo method (see Eq. (16)) is given by the standard parametrization

$$\nu_t = C_\mu \frac{k^2}{\varepsilon}, \quad C_\mu = 0.09. \tag{28}$$

5. Simulation details

The simulations are performed on a 2-d axisymmetric domain extending 77.5 mm in radial and 550 mm in axial direction using the in-house hybrid PDF-RANS solver PDFD [37,41] developed at the Delft University of Technology. The domain is discretized by a non-uniform grid using 69 × 292 (radial by axial) cells. The grid is refined in the shear layer near the nozzle to resolve the strong radial velocity gradients. The DTM grid is created by clustering four FV cells in axial and three FV cells in radial direction and hence a total of 23 × 73 cells are used. From each boundary face of the DTM grid 16,384 rays are traced with equal solid angle increments. The Monte-Carlo method uses 50 particles per cell and an additional averaging over 1000 iteration is performed to smooth the particle mean fields. The boundary conditions are given by:

- **Fuel inlet:**
  The velocity, Reynolds-stress and turbulent kinetic energy dissipation profiles at the nozzle inlet are obtained from separate simulations of the flow through the fuel pipe. The pipe flow simulations are based on bulk velocities of $U_b = 20.3$ m/s and $U_b = 6.77$ m/s for flames P1 and P3, respectively. The enthalpy at the fuel inlet is given by $h = -4656.9$ kJ/kg (corresponding to a fuel temperature $T_f = 295$ K), the mixture fraction is set to $\xi = 1$, the reaction progress variable $Y = 0$ and the soot scalars are set to $N = M = 0$.
- **Air inlet:**
  The air flow through the annulus is given by $\tilde{u}_{ax} = 0.61$ m/s, $\widetilde{u_i''u_j''} = 0.0013\ \mathrm{m}^2/\mathrm{s}^2\delta_{ij}$, $\epsilon = 0.0258\ \mathrm{m}^2/\mathrm{s}^3$ for flame P1 and by $\tilde{u}_{ax} = 0.186$ m/s, $\widetilde{u_i''u_j''} = 10^{-4}\ \mathrm{m}^2/\mathrm{s}^2\delta_{ij}$, $\epsilon = 8 \cdot 10^{-5}\ \mathrm{m}^2/\mathrm{s}^3$ for flame P3. For both flames the scalars are set to $h = -3.1$ kJ/kg (corresponding to an air temperature $T_a = 295$ K), the mixture fraction is set to $\xi = 0$, the reaction progress variable $Y = 0$ and the soot scalars are set to $N = M = 0$.
- **Pyrex wall:**
  No wall model is used and hence simple Neumann boundary condition are applied for all variables. The Pyrex wall temperature is assumed to be $T_w = 300$ K with an emissivity of $\varepsilon_{pw} = 0.7$. Convective heat transfer to the wall is neglected.
- **Outlet:**
  A standard pressure outlet condition (zero gauge pressure, Neumann conditions for all other variables) is used for the FV variables. Particles are removed from the ensemble if the leave the domain.

The steady-state forms of the FV-equations (20)–(22) and (26) are solved numerically in an iterative manner using a pressure-correction algorithm (PISO). A second order upwind scheme is used for the spatial discretization in all equations. The Lagrangian gas particle equations are solved based on a fractional step method [39]. To ensure second order accuracy the “mid-point” rule is used [44] for the time integration. Due to the statistically stationary conditions, a local time stepping algorithm is adopted [45]. This greatly increases the convergence rate since larger particle time steps can be used in regions with small velocities. An average of 50 gas particles per cell is used. To further reduce the statistical error additional iteration averaging has been performed over 1000 iterations [41]. The FV solver and the particle solvers are loosely coupled. This means that an outer iteration consists of 800 FV iterations followed by 10 particle time steps. The implicit DTM equation is solved until the relative change in the total radiative heat transferred in the domain is less than $\epsilon_{DTM} = 10^{-3}$ (usually within three iterations) and is updated every 10th particle time step. About 5000 outer iterations are required to reach a converged solution.

6. Simulation results

6.1. Model validation

Fig. 3 shows the mean mixture fraction $\widetilde{Z}$ (left) and the mean temperature $\widetilde{T}$ (right) (right) along the centerline of flame P1. The simulation results (solid line) are compared to the measurements of Brookes and Moss [11] (circles). The predictions for the mean mixture fraction are in good agreement with the measurements (reported uncertainty of ±6% [11]) indicating that the model predicts overall the correct spreading rate of this round jet flame.

The temperature predictions also show good agreement with the measurements (no uncertainty values reported). The decline of the temperature at the center line after the peak at $x/D \approx 110$ can be attributed to the radiative heat loss since the mean mixture fraction values are still well above the stoichiometric mixture fraction $Z_{st} = 0.055$. Unfortunately, no measurement data is available farther downstream to evaluate the prediction for the radiative heat transfer directly in flame P1. The temperature decrease corresponds well to a region of large soot volume fraction and therefore enhanced thermal radiation as can be seen from the mean soot volume fraction $\widetilde{f_V} = \langle\rho\rangle\widetilde{Y}_s/\rho_{soot}$ shown in Fig. 4. The predicted mean soot volume fraction is in very good agreement with the measured values (reported uncertainty of ±50% [11]). The quality of the predictions is slightly better than the result reported by Consalvi et al. [16] and by Kronenburg et al. [15] both using the soot model of Lindstedt [46]. Consalvi et al. [16] used a hybrid flamelet/stochastic Eulerian field PDF closure with and Kronenburg et al. [15] used a conditional moment closure with detailed methane chemistry. Unfortunately, no experimental data is available beyond $x/D = 105$ so the predicted soot burnout cannot be verified.

Fig. 5 shows radial profiles of the mean mixture fraction $\widetilde{Z}$ compared to the available measurements in flame P1. The agreement at the core of the jet flame is quite good but a small difference between the predicted values and the measurements can be observed at the very edge of the jet flame for downstream positions $x/D \geq 49$ where the simulation results predict a slightly faster spreading of the jet than the experimental values indicate. The difference between the simulation results and the measurements seems to be larger than the measurement uncertainty of 6% as stated by [11].

The effect of the under prediction of the mean mixture fraction at the edge of the jet flame farther downstream can be seen in the radial profiles for the mean temperature shown in Fig. 6. As for the mean mixture fraction, the agreement at the jet core is good but the temperature is consistently under predicted at the edge of the flame for downstream positions $x/D \geq 61$ due to the under predictions of the mixture fractions (lower than stoichiometric). At the edge of the jet, the turbulence is very weak in this low-Re flow and it becomes difficult to model using a simple RANS model with a gradient-diffusion assumption for the scalar fluxes.

Fig. 7 shows radial profiles of the mean soot volume fraction $\widetilde{f_V}$ in comparison with the measurements. The qualitative and quantitative agreement of the FGM results with the measurements is quite good although the experimental profiles appear to be more bulky at $x/D =$ 86,104 than the predicted result. The slow radial decay of soot in the measurements (leading to the bulky profiles) is attributed to an artifact [15] of the curve fitting technique used in [11] that converts the measured extinction profiles into soot volume fraction: the very small soot levels in flame P1 and a high signal-to-noise ratio allowed only a low fourth-order polynomial fit which gives the profiles their bulky shape [15]. Given the accurate predictions of the mean temperature and the mean mixture fraction this result demonstrates that the simple soot model developed by Moss et al. [8] for laminar diffusion flames works very well in turbulent methane–air flames at atmospheric pressure. It should be emphasized that no additional scaling parameters have been introduced as was shown to be necessary in presumed shape PDF simulations [9] of the flame P1.

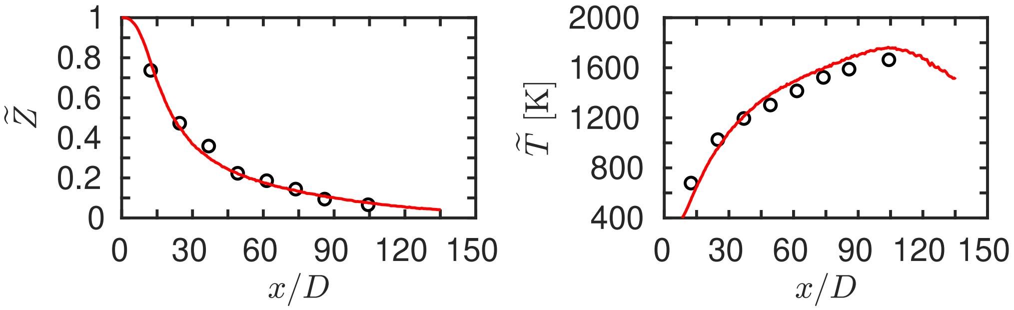

Fig. 3. Axial profiles of mean mixture fraction (left) and mean temperature (right) for flame P1. Solid lines denote simulation results and circles denote measurements [11].

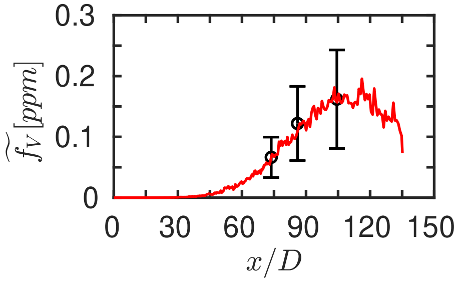

Fig. 4. Axial profile of mean soot volume fraction for flame P1. Solid line denote simulation results and circles denote measurements [11].

The higher pressure flame P3 is a more stringent test for the combustion model, the soot model and the radiation model. The higher soot levels allowed higher order polynomial curve fits to convert the measured extinction profiles into soot volume fraction. Fig. 8 shows axial profile of the mean temperature (left) and mean soot volume fraction (right) for flame P3. Experimental results for the mean mixture fraction in flame P3 are not available. The mean temperature predictions are in good agreement with the measurements although a slight over prediction can be observed. Based on the location of the peak temperature, the flame P3 is significantly shorter than the flame P1 although P3 has the same mass flow rates and the same Reynolds number. The reduced flame length in P3 is due to an increased residence time (lower nozzle exit velocity) and due to larger density gradients which lead to stronger buoyancy production of turbulence and hence to an increase in turbulent mixing. The soot volume fraction in flame P3 is one order of magnitude larger than in flame P1 due to the increased residence time and the combined effect of a larger concentration of C_2H_2 and a reduced concentration of OH [9]. The larger soot volume fraction leads to larger emission of thermal radiation and hence more enthalpy loss in flame P3 as compared to P1. This can be seen by the overall smaller temperatures in P3 and also by the stronger temperature decrease downstream of the peak. The mean soot volume fraction is predicted quite well for $x/D < 61$ but over predicted farther downstream similar to the results presented by [16] who also used a transported PDF with tabulated chemistry modeling approach. The overprediction of the mean soot volume fraction farther downstream could be caused by a too fast soot surface growth mechanism which also causes the peak value to occur farther downstream than in the experiments. We will demonstrate in Section 6.2 that the excessive soot growth is likely caused by a too slow agglomeration mechanism.

Fig. 9 shows radial profiles of the mean temperature at several axial locations in flame P3 (no measurements are available past $X/D = 61$). The predictions are in close agreement with the measurements for $x/D < 37$. Farther downstream, the temperature near the center of the flame is slightly over predicted and an under prediction of the spreading of the temperature profile can be observed similar to the findings for flame P1. The results presented by [16,47] display even higher temperature peaks. Since mean mixture fraction measurements are not available for flame P3 one cannot say for sure that the observed temperature mismatch is due to an incorrect prediction of the jet spreading or due to an underprediction of the radiative heat transfer from the hotter to the colder regions.

The predictions of the mean soot volume fraction $\widetilde{f_V}$ are compared to measurements in Fig. 10. At $x/D = 37$ and $x/D = 49$ the agreement between the results and the measurements is roughly within the measurement uncertainty. Farther downstream $x/D \geq 74$ the qualitative trend is still captured well but the peak values at the jet center are over predicted as discussed above.

6.2. Soot model analysis

The P1 and P3 flames have been studied either using the Brookes and Moss soot model [9,10] or with variations of the Lindstedt soot model [15,16,47]. However, to the best of our knowledge, results of the two soot models have not been compared to each other while keeping all other models unchanged. Here, we compare the Brookes and Moss model (BM) as given in Section 4.1 to the Lindstedt (LS) based model used by Consalvi et al. [16]. One of the main difference is the agglomeration rate parameter which is set to $C_{a,BM} = 1$ in the BM model but $C_{a,LS} = 9$ is used in the LS model. The faster soot particle agglomeration of the LS model causes the soot particle diameter to grow faster which in turn leads to a smaller soot surface area per unit volume for the same soot mass fraction. Therefore, we expect the surface growth and oxidation processes to be slower leading to overall lower values of the mean soot volume fraction. For comparison, we also consider the BM model with $C_a = 9$ (BM-9) and the results are shown in Fig. 11. The mean soot volume fraction results using the LS model and the BM-9 model are almost identical and indeed compare much more favorable to the experimental results. The peak value of the soot volume fraction is now predicted much better although the location of the peak is still too far downstream. Somewhat surprisingly, the 38% reduction in the mean soot volume fraction predicted by the BM-9 and LS models causes only a very small increase in the predicted mean temperature due to the reduced soot thermal radiation contribution. Given the improved predictions with the BM-9 model we will use it to analyze the influence of the mixing time scale next.

6.3. Effect of the soot mixing frequency model

The molecular diffusion of the soot particles is negligible in comparison to the much faster molecular diffusion of gaseous species. In addition, the thermophoretic diffusion of soot was shown to be negligible in a Direct Numerical Simulation (DNS) study of a turbulent flame [48]. The lack of molecular diffusion of soot variables is represented in our modeling approach first by neglecting the mean molecular diffusion term in the scalar equation for the soot variables and second by reducing the micro-mixing frequency of the soot variables by a factor $C_{ms} = 100$. Using such a small mixing frequency is essentially identical to completely neglecting micro-mixing of the

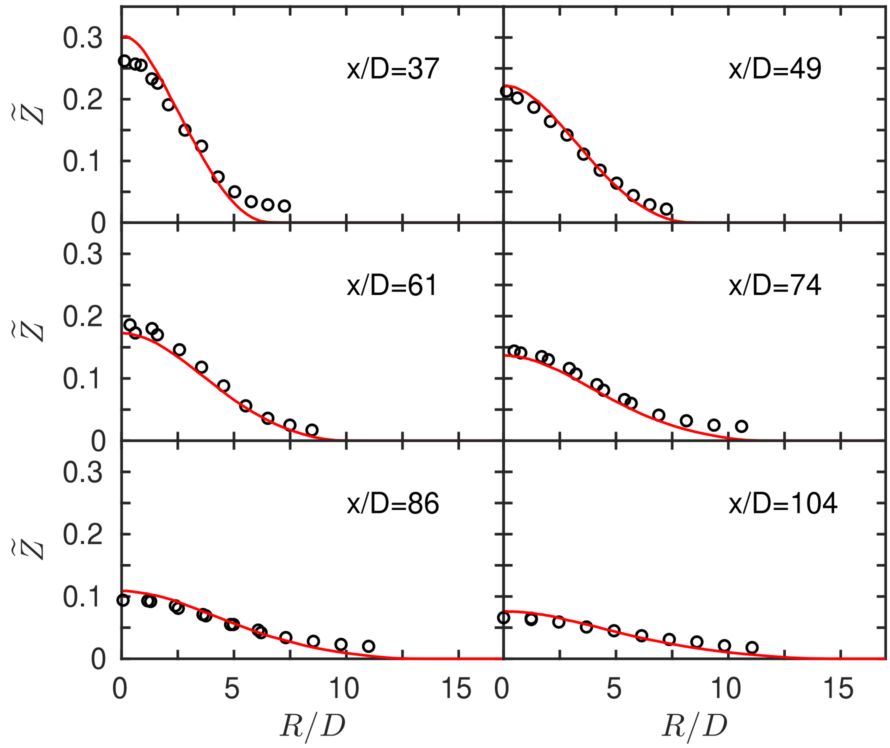

Fig. 5. Radial profiles of mean mixture fraction for flame P1. Solid line denote simulation results and circles denote measurements [11].

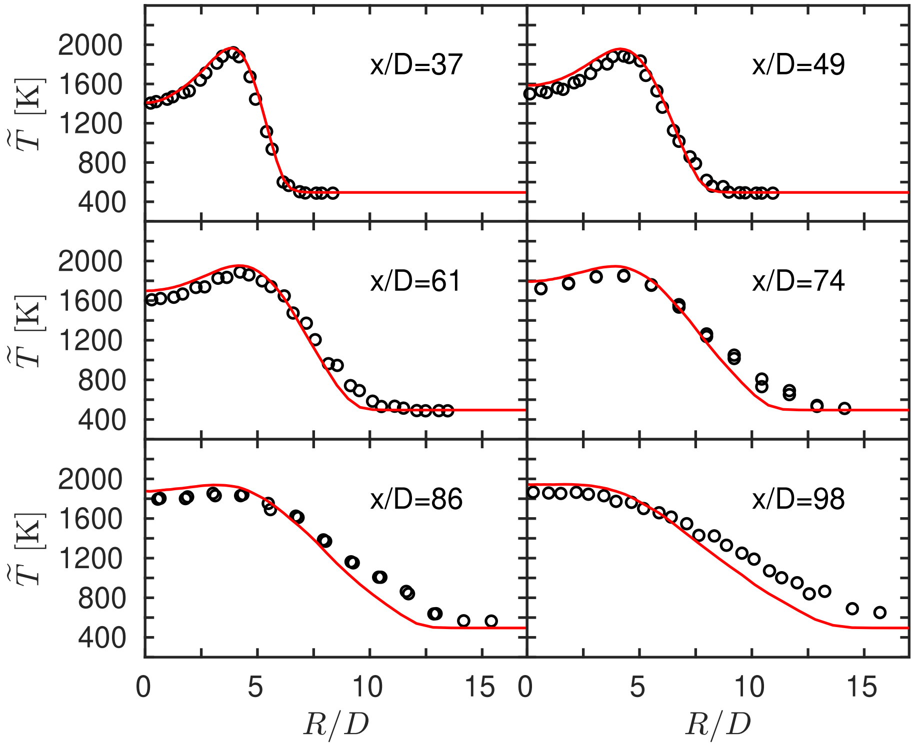

Fig. 6. Radial profiles of mean temperature for flame P1. Solid line denote simulation results and circles denote measurements [11].

soot variables. In previous PDF studies of soot formation micro-mixing has been neglected [10] or has been modeled with the same model as adopted for the gaseous scalars [3,5,13]. To investigate the influence of these choices for the soot micro-mixing we have performed additional simulations with $C_{ms} = 1$ and $C_{ms} = 1000$.

Results are presented in Fig. 12 for the mean temperature (left) and the mean soot volume fraction (right). The mean temperature is not affected at all by the C_{ms} variations. More surprisingly, the mean soot volume fraction is not affected much either: the results for $C_{ms} = 100$, and 1000 are identical (showing that both values correspond to neglecting micro-mixing). Using $C_{ms} = 1$ results in shifting the

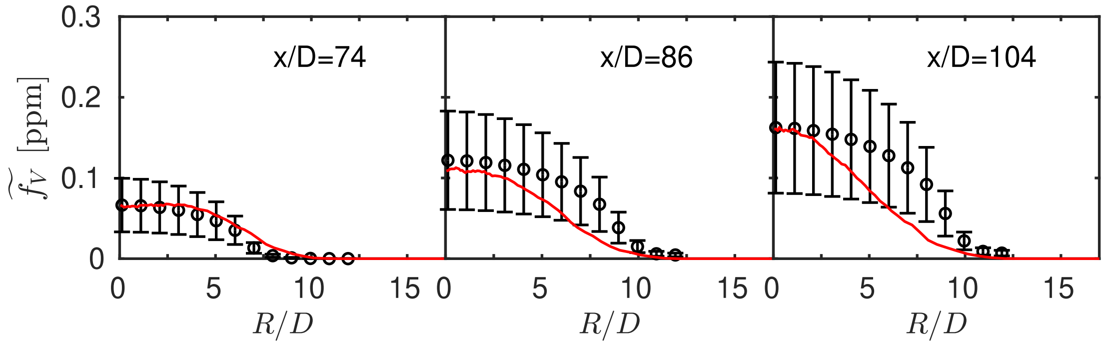

Fig. 7. Radial profiles of mean soot volume fraction for flame P1. Solid line denote simulation results and circles denote measurements [11].

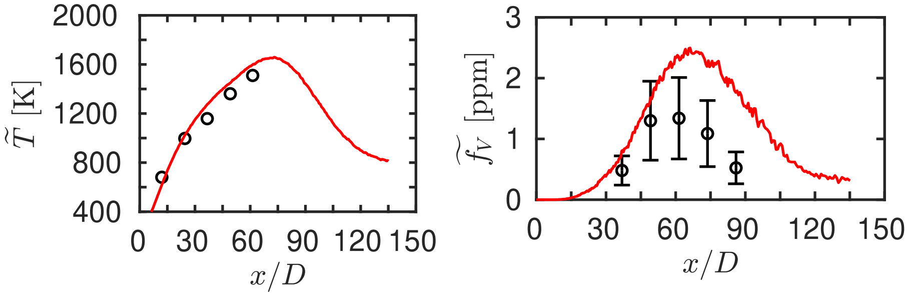

Fig. 8. Axial profiles for flame P3 of mean temperature (left) and mean soot volume fraction (right). Solid lines denote simulation results and circles denote measurements.

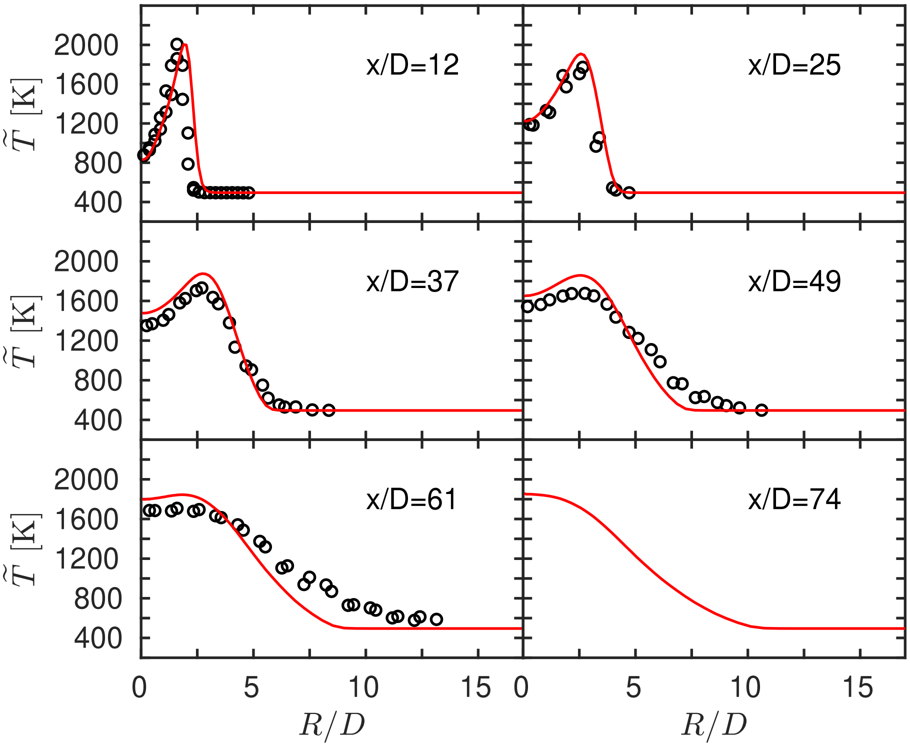

Fig. 9. Radial profiles of mean temperature for flame P3. Solid line denote simulation results and circles denote measurements [11].

entire profile of the soot volume fraction slightly upstream. Keeping the reported measurement uncertainty in mind, the quality of the results for the mean soot volume fraction using $C_{ms} = 1$, and 100 is comparable.

Fig. 13 shows a comparison of scatter plots of the soot volume fraction vs. the mixture fraction at $x/D = 65$ (corresponding to the maximum soot volume fraction) for the $C_{ms} = 100$ case (left) and the $C_{ms} = 1$ case (right). Also shown are the conditional mean and the conditional standard deviation of the soot volume fraction. The $C_{ms} = 100$ results show that almost all soot is formed on the rich side $Z > Z_{st} = 0.055$ with a peak conditional mean at $Z \approx 2Z_{st}$. Large scattering can be observed and hence the conditional standard deviation of the soot volume fraction is nearly as large as the conditional mean. These trends are characteristic of soot formation in turbulent flames as shown in DNS [48] and LES [13] studies. The trends are quite different in the

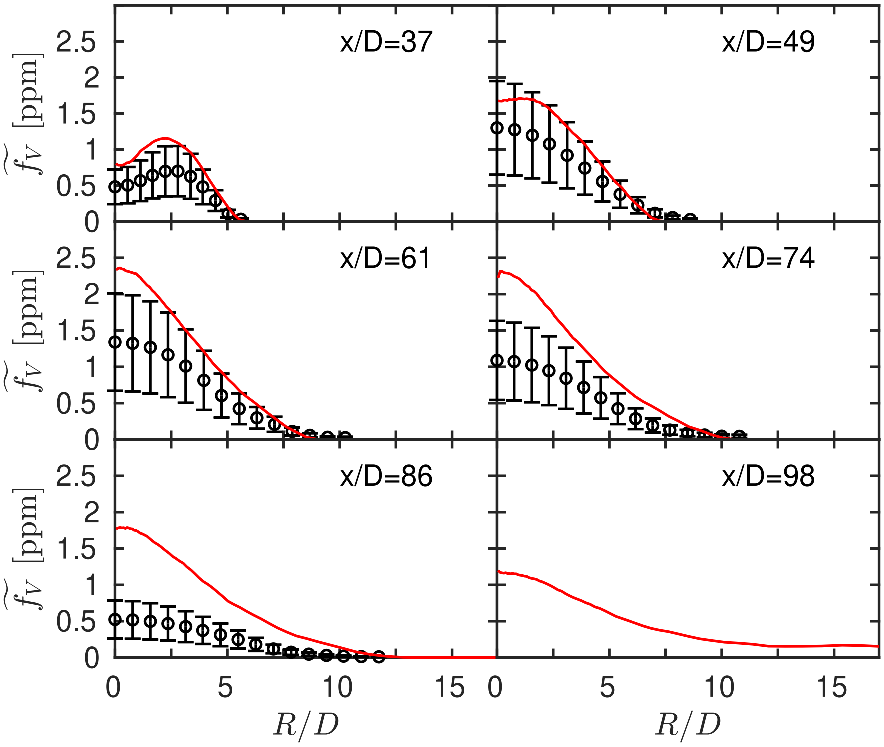

Fig. 10. Radial profiles of mean soot volume fraction for flame P3. Solid line denote simulation results and circles denote measurements [11].

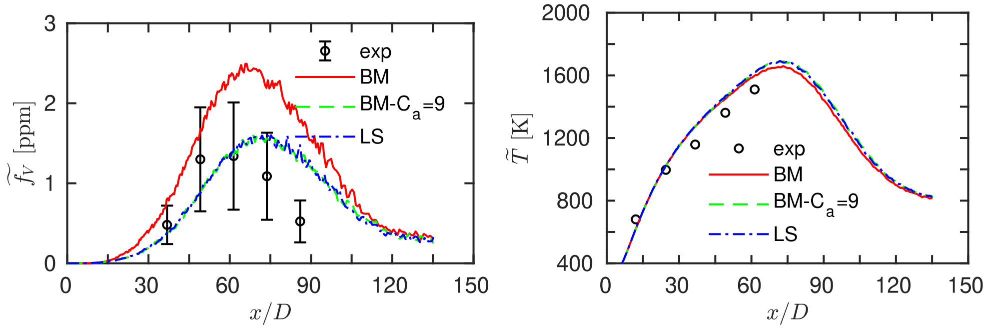

Fig. 11. Comparison of soot model results using the Brookes and Moss model (red solid line), the Brookes and Moss model with $C_a = 9$ (green dashed line), and the Lindstedt model (blue dashed–dotted line). Axial profiles for flame P3 of mean soot volume fraction (left) and mean temperature (right). Solid lines denote simulation results and circles denote measurements.

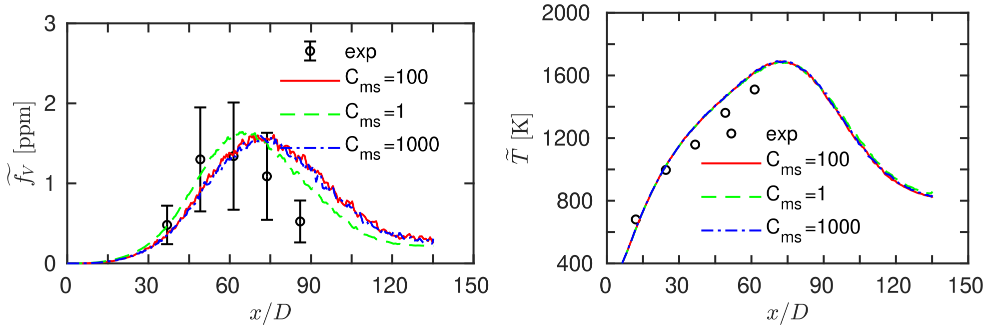

Fig. 12. Axial profiles for flame P3 of mean temperature (left) and mean soot volume fraction (right) obtained with different soot mixing frequencies: $C_{ms} = 1$ (green dashed line), $C_{ms} = 100$ (red solid line) and $C_{ms} = 1000$ (blue dash–dot line).

$C_{ms} = 1$ case (left): soot can be found for $Z < Z_{st}$ (due to micro-mixing) and much less scattering is observed. Therefore, using $C_{ms} = 100$ produces more realistic results that are in qualitative agreement with DNS and LES data.

It should be noted that the Conditional Moment Closure studies of the same flames by Kronenburg et al. [15] and by Woolley et al. [47] indicated a much larger sensitivity of the mean soot volume fraction on the differential diffusion model. Based on the very large conditional

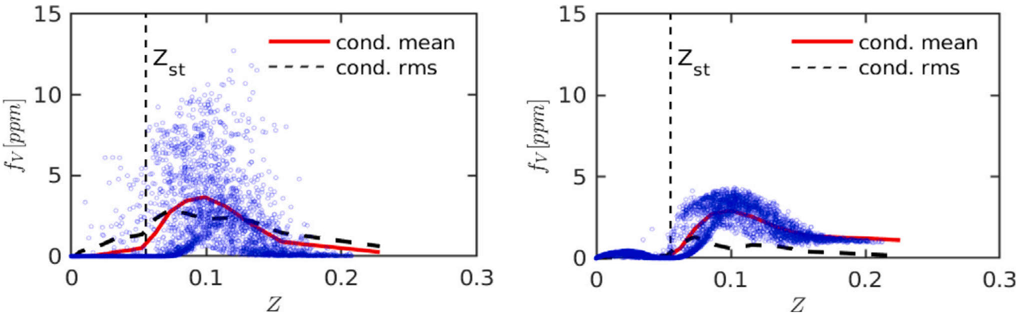

Fig. 13. Scatter plot of soot volume fraction, conditional means (solid line) and conditional standard deviations (dashed line) at $x/D = 65$ for $C_{ms} = 100$ (left) and $C_{ms} = 1$ (right).

standard deviation of the soot volume fraction observed here and elsewhere [13,48], the validity of a first order conditional moment closure approach to predict soot formation has to be questioned.

7. Conclusions

The effect of radiative heat loss on the chemical composition can be significant in sooting flames. Using a Flamelet Generated Manifold chemistry model including heat loss/gain allows to account for this effect. The accuracy of the FGM method is analyzed quantitatively by using flamelet solutions that are not included in the generating set of the FGM and we found the progress variable source term to have the largest errors but remaining below 6%.

In this work, the FGM chemistry and a simple semi-empirical soot model are used within the transported scalar PDF method. We consider methane flames at atmospheric conditions (flame P1) and at three bar pressure (flame P3) [11] for model validation. The soot volume fraction in these flames is moderate and thus the non-gray gas radiation is accounted for by using a non-gray weighted sum of gray gases (WSGG) model. With the adopted transported PDF closure we are able to account for turbulence–radiation interaction at the level of the optically thin fluctuation approximation. Simulation results for the atmospheric flame P1 are in excellent agreement with the measurements. The good agreement demonstrates that a simple semi-empirical soot model that was developed for laminar flames can be adopted to turbulent flames of the same fuel without any additional modifications given that the chemistry and the turbulence–chemistry interaction, the thermal radiation and the differential diffusion of soot are modeled sufficiently accurately.

The simulation results for the three bar pressure flame P3 over predicted the mean soot volume fractions. The adopted Brookes and Moss (BM) soot model was calibrated for atmospheric pressure and some uncertainty about the model parameters at higher pressures exist [9]. We have compared the results for P3 using the BM model with the more commonly adopted semi-empirical soot model of Lindstedt [46] (LS) and found the latter to provide better agreement with the measurements. A main difference between the BM and LS model is the increased agglomeration rate parameter in the LS model. Indeed, when using the LS agglomeration rate parameter value $C_a = 9$ in the BM model, results drastically improved and are essentially identical to the LS model results.

A simple model that accounts for the negligible molecular mixing by significantly reducing the mixing frequency of the soot variables is proposed in this work. Reducing the mixing frequency by a factor $C_{ms} = 100$ is essentially equal to neglecting the micro-mixing and is found to provide good quantitative results for the mean soot volume fraction. Using the same mixing model for the soot variables as for the gaseous variables (i.e. $C_{ms} = 1$) does not have a large effect on the predictions of the mean soot volume fraction. However, by comparing qualitatively the trends of the conditional mean and conditional standard deviation of the soot volume fraction (conditional on the mixture fraction) to DNS [48] and LES data [13] of non-premixed flames shows that the "no micro-mixing" ($C_{ms} = 100$) assumption is more realistic. Hence, for future PDF studies of soot formation it is recommended that the soot variables should not participate in micro-mixing.

Declaration of competing interest

The authors declare the following financial interests/personal relationships which may be considered as potential competing interests: Dirk Roekaerts reports financial support was provided by Technology Foundation STW. Michael Stoellinger reports financial support was provided by University of Wyoming School of Energy Resources.

Acknowledgments

This work has been financially supported in part by the Dutch Technology Foundation (STW) and in part by the School of Energy Resources at the University of Wyoming. We would like to thank the reviewers for their valuable suggestions to improve the paper.

References

[1] Frenklach M, Wang H. Detailed modeling of soot particle nucleation and growth. Proc Combust Inst 2001;23:1559–66.

[2] Appel J, Bockhorn H, Frenklach M. Kinetic modeling of soot formation with detailed chemistry and physics: laminar premixed flames of C2 hydrocarbons. Combust Flame 2000;121(1–2):122–36.

[3] Mehta R, Haworth D, Modest M. An assessment of gas-phase reaction mechanisms and soot models for laminar atmospheric-pressure ethylene–air flames. Proc Combust Inst 2009;32(1):1327–34.

[4] El-Asrag H, Menon S. Large eddy simulation of soot formation in a turbulent non-premixed jet flame. Combust Flame 2009;156(2):385–95. http://dx.doi.org/10.1016/j.combustflame.2008.09.003, URL https://www.sciencedirect.com/science/article/pii/S0010218008002769.

[5] Lindstedt R, Louloudi S. Joint-scalar transported PDF modeling of soot formation and oxidation. Proc Combust Inst 2005;30(1):775–83.

[6] Mehta R, Haworth D, Modest M. Composition PDF/photon Monte Carlo modeling of moderately sooting turbulent jet flames. Combust Flame 2010;157(5):982–94.

[7] Rigopoulos S. Effect of precursors and radiation on soot formation in turbulent diffusion flame. Flow Turbul Combust 2019;103:565–604. http://dx.doi.org/10.1007/s10494-019-00054-8.

[8] Moss JB, Stewart CD, Young KJ. Modeling soot formation and burnout in a high temperature laminar diffusion flame burning under oxygen-enriched conditions. Combust Flame 1995;101(4):491–500.

[9] Brookes S, Moss J. Predictions of soot and thermal radiation properties in confined turbulent jet diffusion flames. Combust Flame 1999;116(4):486–503.

[10] Aksit I, Moss J. A hybrid scalar model for sooting turbulent flames. Combust Flame 2006;145(1–2):231–44.

[11] Brookes SJ, Moss JB. Measurements of soot production and thermal radiation from confined turbulent jet diffusion flames of methane. Combust Flame 1999;116(1–2):49–61.

[12] van Oijen JA, Lammers FA, de Goey LPH. Modeling of complex premixed burner systems by using flamelet-generated manifolds. Combust Flame 2001;127(3):2124–34.

[13] Donde P, Raman V, Mueller ME, Pitsch H. LES/PDF based modeling of soot-turbulence interactions in turbulent flames. Proc Combust Inst 2013;34(1):1183–92.

[14] Lockwood FC, Shah NG. A new radiation solution method for incorporation in general combustion prediction procedures. Symp (International) Combust 1981;18:1405–14, The Combustion Institute.

[15] Kronenburg A, Bilger R, Kent J. Modeling soot formation in turbulent methane–air jet diffusion flames. Combust Flame 2000;121(1–2):24–40.

[16] Consalvi J-L, Nmira F, Burot D. Simulations of sooting turbulent jet flames using a hybrid flamelet/stochastic Eulerian field method. Combust Theory Model 2016;20(2):221–57. http://dx.doi.org/10.1080/13647830.2015.1125024.

[17] Carbonell D, Perez-Segarra C, Coelho P, Oliva A. Flamelet mathematical models for non-premixed laminar combustion. Combust Flame 2009;156(2):334–47. http://dx.doi.org/10.1016/j.combustflame.2008.07.011, URL https://www.sciencedirect.com/science/article/pii/S0010218008002289.

[18] Sanders J, Sarh B, Gökalp I. Variable density effects in axisymmetric isothermal turbulent jets: a comparison between a first- and a second-order turbulence model. Int J Heat Mass Transfer 1997;40(4):823–42.

[19] Egüz U, Leermakers N, Somers B, de Goey P. Modeling of PCCI combustion with FGM tabulated chemistry. Fuel 2014;118:91–9. http://dx.doi.org/10.1016/j.fuel.2013.10.073, URL https://www.sciencedirect.com/science/article/pii/S0016236113010223.

[20] Efimov DV, de Goey P, van Oijen JA. Qfm: quenching flamelet-generated manifold for modelling of flame–wall interactions. Combust Theory Model 2020;24(1):72–104. http://dx.doi.org/10.1080/13647830.2019.1658901.

[21] Donini A, Bastiaans R, van Oijen J, de Goey L. A 5-D implementation of FGM for the large eddy simulation of a stratified swirled flame with heat loss in a gas turbine combustor. Flow Turbul Combust 2017;98:887–922. http://dx.doi.org/10.1007/s10494-016-9777-7.

[22] Smith GP, et al. Gri-mech 3.0. 1995, https://www.me.berkeley.edu/grimech.

[23] Peters N. Turbulent combustion. Cambridge, UK: Cambridge University Press; 2000.

[24] Ihme M, Pitsch H. Modeling of radiation and nitric oxide formation in turbulent nonpremixed flames using a flamelet/progress variable formulation. Phys Fluids 2008;20(5):055110.

[25] Sandia National Laboratories. TNF Workshop website. Tech. Rep., TNF; 2003, URL https://www.ca.sandia.gov/TNF/radiation.html.

[26] CHEM1D. A one-dimensional laminar flame code. Eindhoven University of Technology; 2006, https://www.combustion.tue.nl/chem1d.

[27] Peeters T. Numerical modeling of turbulent natural-gas diffusion flames. (Ph.D. thesis), Technische Universiteit Delft; 1995.

[28] Verhoeven L, Ramaekers W, van Oijen J, de Goey L. Modeling non-premixed laminar co-flow flames using flamelet-generated manifolds. Combust Flame 2012;159(1):230–41. http://dx.doi.org/10.1016/j.combustflame.2011.07.011, URL https://www.sciencedirect.com/science/article/pii/S0010218011002239.

[29] Reddy M, De A, Yadav R. Effect of precursors and radiation on soot formation in turbulent diffusion flame. Fuel 2015;148:58–72.

[30] Liu F, Consalvi J-L, Coelho PJ, Andre F, Gu M, Solovjov V, et al. The impact of radiative heat transfer in combustion processes and its modeling – with a focus on turbulent flames. Fuel 2020;281:118555. http://dx.doi.org/10.1016/j.fuel.2020.118555, URL https://www.sciencedirect.com/science/article/pii/S0016236120315519.

[31] Centeno FR, Brittes R, Rodrigues LG, Coelho FR, França FH. Evaluation of the WSGG model against line-by-line calculation of thermal radiation in a non-gray sooting medium representing an axisymmetric laminar jet flame. Int J Heat Mass Transfer 2018;124:475–83. http://dx.doi.org/10.1016/j.ijheatmasstransfer.2018.02.040, URL https://www.sciencedirect.com/science/article/pii/S0017931017350561.

[32] Sadeghi H, Hostikka S, Fraga GC, Bordbar H. Weighted-sum-of-gray-gases models for non-gray thermal radiation of hydrocarbon fuel vapors, CH4, CO and soot. Fire Saf J 2021;125:103420. http://dx.doi.org/10.1016/j.firesaf.2021.103420, URL https://www.sciencedirect.com/science/article/pii/S0379711221001612.

[33] Hottel H, Sarofim A. Radiative transport. New York: McGraw Hill; 1967.

[34] Modest MF. The weighted-sum-of-gray-gases model for arbitrary solution methods in radiative transfer. J Heat Transfer 1991;113(3):650–6. http://dx.doi.org/10.1115/1.2910614.

[35] Bordbar MH, Wecel G, Hyppänen T. A line by line based weighted sum of gray gases model for inhomogeneous CO2-H2O mixture in oxy-fired combustion. Combust Flame 2014;161(9):2435–45. http://dx.doi.org/10.1016/j.combustflame.2014.03.013, URL https://www.sciencedirect.com/science/article/pii/S0010218014000935.

[36] Coelho P. Numerical simulation of the interaction between turbulence and radiation in reactive flows. Prog Energy Combust Sci 2007;33(4):311–83.

[37] Stoellinger M, Naud B, Roekaerts D, Beishuizen N, Heinz S. PDF modeling and simulations of pulverized coal combustion – part 1: Theory and modeling. Combust Flame 2013;160(2):384–95.

[38] Coelho PJ, Carvalho MG. A conservative formulation of the discrete transfer method. Trans ASME 1997;119:118–28.

[39] Pope S. PDF methods for turbulent reactive flows. Prog Energy Combust Sci 1985;11(2):119–92.

[40] Haworth D. Progress in probability density function methods for turbulent reacting flows. Prog Energy Combust Sci 2010;36(2):168–259.

[41] Naud B, Jiménez C, Roekaerts D. A consistent hybrid PDF method: implementation details and application to the simulation of a bluff-body stabilised flame. Prog Comput Fluid Dyn 2006;6:147–57.

[42] Launder BE. Second-moment closure and its use in modeling turbulent industrial flows. Internat J Numer Methods Fluids 1989;9:963–85.

[43] Pope SB. An explanation of the turbulent round-jet/plane-jet anomaly. AIAA J 1978;16:279–81.

[44] Muradoglu M, Pope SB, Caughey DA. The hybrid method for the PDF equations of turbulent reactive flows: Consistency conditions and correction algorithms. J Comput Phys 2001;172(2):841–78.

[45] Muradoglu M, Pope S. Local time-stepping algorithm for solving the probability density function turbulence model equations. AIAA J 2002;40(9):1755–63.

[46] Lindstedt PR. Simplified soot nucleation and surface growth steps for non-premixed flames. In: Bockhorn H, editor. Soot formation in combustion: mechanisms and models. Berlin, Heidelberg: Springer Berlin Heidelberg; 1994, p. 417–41. http://dx.doi.org/10.1007/978-3-642-85167-4_24.

[47] Woolley RM, Fairweather M, Yunardi. Conditional moment closure modelling of soot formation in turbulent, non-premixed methane and propane flames. Fuel 2009;88(3):393–407. http://dx.doi.org/10.1016/j.fuel.2008.10.005, URL https://www.sciencedirect.com/science/article/pii/S0016236108003967.

[48] Lignell DO, Chen JH, Smith PJ. Three-dimensional direct numerical simulation of soot formation and transport in a temporally evolving nonpremixed ethylene jet flame. Combust Flame 2008;155(1–2):316–33.